IEEE Access
Multidisciplinary | Rapid Review | Open Access Journal

Received 17 August 2022, accepted 4 September 2022, date of publication 12 September 2022,
date of current version 23 September 2022.

*Digital Object Identifier 10.1109/ACCESS.2022.3206357*

RESEARCH ARTICLE

# Design and Characterization of Self-Shielded MRI Gradient Coils With Finite Track Width

**SADEQ S ALSHARAFI, (Member, IEEE), HAILE BAYE KASSAHUN, AHMED M BADAWI, (Senior Member, IEEE), AND ABDEL-MONEM M EL-SHARKAWY, (Member, IEEE)**
Department of Systems and Biomedical Engineering, Faculty of Engineering, Cairo University, Giza, Egypt

Corresponding author: Sadeq S Alsharafi (s.alsharafi@eng-st.cu.edu.eg)

Sadeq Alsharafi is partially financially supported for his Ph.D. program at Cairo University by the Yemeni ministry of higher education. Haile Kassahun is financially supported by the African Biomedical Engineering Mobility (ABEM) for his Ph.D. program at Cairo University. The ABEM project is funded by the Intra-Africa Academic Mobility Scheme of the Education, Audiovisual, and Culture Executive Agency of the European Commission. All programming and simulations were performed by Sadeq S Alsharafi.

**ABSTRACT** Gradient coils are essential for the performance of magnetic resonance imaging systems. Usually, coils are designed assuming thin wire tracks. Here, we design an MR gradient coil set using a more general approach considering the exact track width using the discrete wire approach. The effect of track width on the DC current density distribution and resultant magnetic fields using both loop and Golay coils are first demonstrated. Both, self-shielded X and Z gradient coils of definite width/thickness are designed and optimized. The resistance and inductance of the coils are calculated using the stream functions approach. Track current distribution was used to compute the magnetic fields over the desired volume, and at the cryostat. The linearity of the magnetic field over the volume, the figure of power, and the shielding ratio of the coil are used as parameters in the optimization process. The DC characteristics of the designed coils with definite (small) track width and thickness were compared for verification to that of the corresponding thin wire design where they were found to have approximately similar characteristics. Using our design methodology, the coils' frequency-dependent resistances and inductances were directly/efficiently calculated. The harmonic and transient eddy current interactions between the longitudinal and transverse gradient coils were computed where track slitting was employed to reduce such interactions. This work stresses the importance of considering coil track width in the design process particularly for wide tracks as well as computing the coil's figure of merit, harmonic and transient coil characteristics/interactions.

**INDEX TERMS** MRI gradient coils, transverse and longitudinal gradient coils, stream functions, eddy currents, harmonics, transient analysis.

## I. INTRODUCTION

The gradient coils have an essential role in MR imaging as they are used to encode the MRI signal in the body by creating a linearly varying magnetic field $B_z$ along the x, y, and z axes [1], [2], Fig.1.

They are commonly designed by one of two methods [3], [4]: the discrete wire method, and the continuous current distribution method.

In the discrete wire method [5], [6], [7], [8], [9], the gradient coil turns of specific geometry (e.g., circle, ellipse, semi-elliptic, etc.) and different sizes are positioned on the surface of two cylinders (one for primary and the other for shielding coil). The size and the position of the turns are iteratively adjusted through a computerized algorithm until specific target fields on the Diameter of Spherical Volume (DSV) and the cryostat are obtained.

In the continuous current distribution method [10], [11], [13], [14], [15], [16], the target fields on the DSV and the cryostat are predefined where the desired target field ($B_z$) components on DSV satisfy the gradient linearity constraint

The associate editor coordinating the review of this manuscript and approving it for publication was Jinhua Sheng.

and the magnetic fields at the cryostat should be as small as possible. The current distribution on the self-shielded gradient coil surfaces may be presented by discrete unknown stream functions on the two cylindrical surfaces. The relationship between the stream functions and the target fields is defined by a linear system that combines the unknown stream functions and the desired target field (on the DSV and cryostat). The stream functions are determined and approximated to contours which represent the discrete gradient coil turns.

Although the continuous gradient design method is efficient where the current distribution is approximated by irregular coil turns, it is accompanied with ill-posed matrices and requires using regularizing approaches in order to obtain an accurate solution. On the contrary, in the discrete wire method, the turns are based on specific smooth curvature geometries which are easier to manufacture. Calculating the magnetic field from the gradient coil, using Biot-Savart's law [17], [18], [19], commonly considers the coil's turns as thin wires. The Biot-Savart's law in terms of line currents is given as:

$$\vec{B} = \frac{\mu_0 I}{4\pi} \int_C \frac{\overrightarrow{dl} \times \overrightarrow{R}}{R^3} \tag{1}$$

where $\vec{B}$ is the magnetic field, $\overrightarrow{R}$ is the vector from the coil segment to the target field point, and $R$ is the length of the vector ($\overrightarrow{R}$), $\overrightarrow{dl}$ is the element vector along the coil path C, $I$ is the line current that passes in the coil, and $\mu_0$ is the permeability of free space which equals $4\pi \times 10^{-7}$ H m$^{-1}$.

Commonly, the gradient coil is assumed to have a thin-wire conductor. In reality, coils are not composed of thin wires but they have definite widths as discussed in [20] and [21] and evident from images of gradient coil structures used by some MRI scanner manufacturers whose exact parameters are not necessarily published. In this paper, we investigate the importance of considering the coil's track width. We exploited the advantage of the discrete wire method to design gradient coils considering the track width and thickness of the coil's turns. The tracks of the coil are meshed into structured triangular elements and the current density on the coil's tracks is represented in terms of the stream functions [22], [23], [24], [25], [26], [27]. Calculating the stream functions is followed by calculating the current density on the coil tracks as well as the frequency-dependent resistance and inductance of the coil which are impossible to be achieved in the case of thin wire assumption. From the calculated current distribution density on the coil tracks, the magnetic field on the DSV and the cryostat cylinder are calculated [28]. Also, cross coil eddy current interaction is calculated where it is shown that track slitting reduces such effects as recommended in [22]. We stress in this work that the X, Y, and Z gradient coil sets affect each other and this is to be considered in coil design in general.

## II. METHODS

The self-shielded gradient coil is represented by two separated concentric cylinders, Fig.1 (a). For the Z gradient coil,

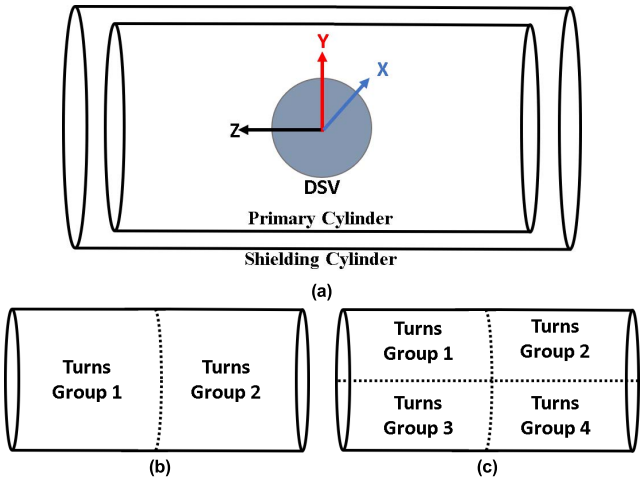


**FIGURE 1.** Illustration showing the two concentric cylinders which hold the primary and the shielding gradient coils (a). Symmetrical turn groups on each cylinder for the Z gradient coil (b) and the transverse gradient coil (c).

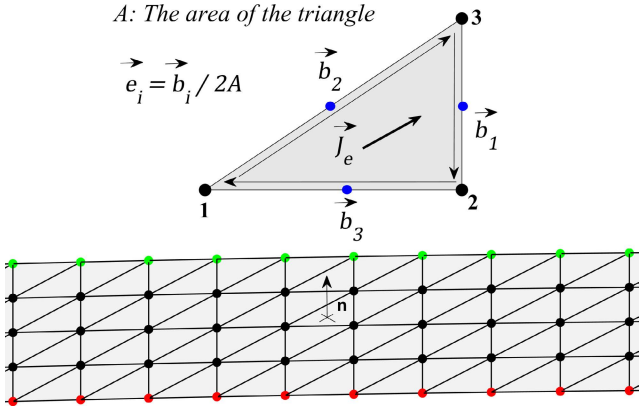


**FIGURE 2.** A turn segment track meshed into structured triangular elements showing the boundary nodes (green and red), internal nodes (blacks), and the integration points at a triangle (blue).

each cylinder is divided transversely into two identical halves, Fig.1 (b). Four groups of turns are arranged on the cylinders: two groups on the inner cylinder for the primary coil and the other two in the outer cylinder for the secondary (shielding) coil. However, For the transverse (X gradient) coil, each cylinder is divided into four identical quadrants, Fig.1 (c). Eight groups of turns, of specific track width and thickness, are arranged on the two cylinders: four groups on the inner cylinder and the other four on the outer cylinder.

Each turn's track is meshed into a single layer of structured triangular elements, Fig.2. The nodes in a triangle are locally numbered from 1 to 3 and globally numbered by unique numbers. The direction of local numbering must be consistent (clockwise or counterclockwise) for all triangles in all turns' tracks. According to the continuity equation and using the stream functions [24], [26], [27], [29], the surface current density $\overrightarrow{J_s}$ on the coil is represented by the stream functions $\Phi$ as:

$$\nabla \times \overrightarrow{J_s} = 0 \tag{2}$$

$$\overrightarrow{J_s} = \nabla \times (\Phi . \hat{n}) \tag{3}$$

where $\hat{n}$ is the normal vector to the surface of the turn track. The surface current density $\overrightarrow{J_e}$ (A/m) inside a triangle element can be given as:

$$\overrightarrow{J_e} = \overrightarrow{e_1}\phi_1 + \overrightarrow{e_2}\phi_2 + \overrightarrow{e_3}\phi_3 \tag{4}$$

where $\overrightarrow{e_1}$, $\overrightarrow{e_2}$, and $\overrightarrow{e_3}$ are the vectors facing the triangle nodes ($\vec{b}_1$, $\vec{b}_2$, and $\vec{b}_3$) divided by the double area of the triangle as depicted in Fig.2. $\phi_1, \phi_2$, and $\phi_3$ are the value of the stream functions at the nodes of the triangle. The volume eddy currents density $\vec{J}$ (A/m$^2$) can be calculated from the division of the surface current density by the thickness of the triangular element (triangular elements have the thickness $t$ of the turn track).

In each turn, the circuit equation (in the time domain and frequency domain) is derived from the total electromagnetic energy by applying the finite element method [24], [26], [27], [29] and it can be given as:

$$\boldsymbol{R\Phi} + \boldsymbol{M}\frac{\partial \boldsymbol{\Phi}}{\partial t} = 0 \quad \text{(time-domain)} \tag{5}$$

$$(\boldsymbol{R} + j\omega\boldsymbol{M})\,\boldsymbol{\Phi} = 0 \quad \text{(frequency-domain)} \tag{6}$$

where $\boldsymbol{\Phi}$ is a vector that contains the stream functions of all nodes on the turn. $\boldsymbol{R}$ and $\boldsymbol{M}$ are the resistance and the inductance matrices due to the interaction of all possible pairs of nodes $n$ and $m$ on the turn.

The impedance matrix $\boldsymbol{Z}$ can be given as:

$$\boldsymbol{Z} = \boldsymbol{R} + j\,\omega\,\boldsymbol{M} \tag{7}$$

where $\omega$ is the angular frequency and $j$ is the imaginary unit.

If the nodes $n$ and $m$ are shared among the group of triangles $N$ and $M$, respectively, then the resistance element $R_{nm}$ and inductance element $M_{nm}$ can be given as:

$$R_{nm} = \frac{1}{\sigma t}\sum_N\sum_M\int_s \vec{e}_{nN}\cdot\vec{e}_{mM}\,ds \tag{8}$$

$$M_{nm} = \frac{\mu_0}{4\pi}\sum_N\sum_M\int_{s'}\int_s \frac{\vec{e}_{nN}\cdot\vec{e}_{mM}}{|\vec{r}_N - \vec{r}_M|}\,ds\,ds' \tag{9}$$

where $\sigma$ and $t$ are the conductivity and the thickness of the turn. The resistance element $R_{nm} = 0$ for the nodes $n$ and $m$ that do not share the same triangle(s). The vectors $\vec{r}_N$ and $\vec{r}_M$ are pointing to the triangular elements in $N$ and $M$ with the areas of $ds$ and $ds'$, respectively. The vectors can be considered to point to the centroids of the triangles, the length $|\vec{r}_N - \vec{r}_M|$ is then simply the central difference between the two centroids of the triangles $N$ and $M$. However, for more accuracy and to reduce singularities, a 3-points distance calculation [30] is used. In this paper, the three points are selected in the middle of the edges of the triangle, as shown in Fig.2. The double integral in equation (9) can be rewritten as:

$$\int_{s'}\int_s \frac{1}{|\vec{r}_N - \vec{r}_M|}\,ds\,ds' = A_N\,A_M\sum_{p=1}^{3}\frac{1}{|\vec{r}_N - \vec{r}_{M_p}|}w_p \tag{10}$$

The vector $\vec{r}_N$ is pointing to the centroid of the triangle, with an area $A_N$, in the group of triangles $N$. The vector $\vec{r}_{M_p}$ is pointing to the point $p$ on the middle edge of the triangle, with an area $A_M$ in group $M$. The weight $w_p$ is associated with point $p$ which in our work is considered to be equal to 1/3. In the case that the nodes $n$ and $m$ belong to the same triangle ($N = M$), a closed form of the double integral is used as described in [26].

The total current $I$ that passes in the turn track is equal to the difference between the values of stream functions of the boundaries of the turn. As shown in Fig.2, the stream functions of the first boundary nodes depicted by the red color are set to zeroes (for simplicity) while the stream functions of the boundary nodes with green are set to the value of current $I$. To reverse the current direction, the setting of stream functions for boundary nodes is simply exchanged. The turn track has two categories of stream functions: the stream function vector $\boldsymbol{\Phi_b}$ for the boundary nodes (they are known and forced to have certain values as discussed in the above setting) and the stream function vector for the internal nodes $\boldsymbol{\Phi_i}$ (they are unknown and need to be solved). By breaking down the stream functions vector $\boldsymbol{\Phi}$ and impedance matrix $\boldsymbol{Z}$ into a combination of the internal and boundary nodes, the circuit equation (6) can be rewritten as:

$$\begin{bmatrix} \boldsymbol{Z_{bb}} & \boldsymbol{Z_{ib}^T} \\ \boldsymbol{Z_{ib}} & \boldsymbol{Z_{ii}} \end{bmatrix}\begin{bmatrix} \boldsymbol{\Phi_b} \\ \boldsymbol{\Phi_i} \end{bmatrix} = \begin{bmatrix} \boldsymbol{0} \\ \boldsymbol{0} \end{bmatrix} \tag{11}$$

where $\boldsymbol{Z_{ii}}$, $\boldsymbol{Z_{bb}}$, and $\boldsymbol{Z_{ib}}$ are the impedance sub-matrices associated with the internal/internal, boundary/boundary, and the internal/boundary nodes of the turn's track, respectively. The solution to the internal stream functions is given as:

$$\boldsymbol{\Phi_i} = -\boldsymbol{Z_{ii}^{-1}}\,\boldsymbol{Z_{ib}}\,\boldsymbol{\Phi_b} \tag{12}$$

The current density can be computed from the stream function values using equation (4).

For a turn, the calculated $\boldsymbol{\Phi_i}$ and $\boldsymbol{\Phi_b}$ are concatenated to create the vector $\boldsymbol{\Phi}$. The per turn resistance $R_t$ and inductance $L_t$ are calculated using the following formulas as directly inferred from the definition of the electrical and magnetic energies in [27]:

$$R_t = \frac{\boldsymbol{\Phi^T}\,\boldsymbol{R}\,\boldsymbol{\Phi}}{I^2} \tag{13}$$

$$L_t = \frac{\boldsymbol{\Phi^T}\,\boldsymbol{M}\,\boldsymbol{\Phi}}{I^2} \tag{14}$$

The above equations are valid for solid turn track, Fig.3 (a). However, it is beneficial to study also the turn with a slitted track, Fig.3 (b). Slitting the turn track into sub-tracks plays important role in reducing the eddy current induced on the turn. In the slitted turn track, Fig.3 (b), the assignment of upper and lower boundary nodes $\boldsymbol{\Phi_b}$ (green and red) is applied as previously discussed with solid turn. To prevent the current from crossing the boundary of slits, a boundary condition is set where the stream functions of the slits' nodes (cyan and yellow) should be equal to an unknown value that needs to be determined. The stream functions of the slits' nodes

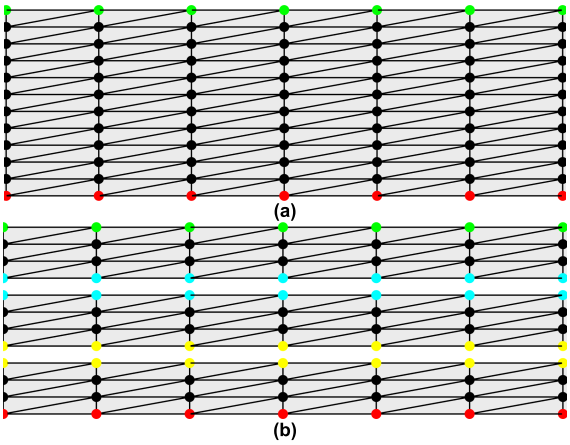


**FIGURE 3.** A solid track mesh (a) with the boundary nodes (green and red) and internal nodes (black). A slitted track mesh (b) shows also the slits' nodes (cyan and yellow).

are included in the vector $\boldsymbol{\Phi_i}$ which is suitably transformed to $\boldsymbol{\Phi_i^0}$ that only contains the independent unknown stream functions. The transformation is done using a transformation matrix $\boldsymbol{H}$ [27] which satisfies the following:

$$\boldsymbol{H}\,\boldsymbol{\Phi_i^0} = \boldsymbol{\Phi_i} \tag{15}$$

The matrix $\boldsymbol{H}$ is a binary matrix with a dimension of $N_{nodes} \times N_{ind}$. $N_{nodes}$ is the number of all nodes on the turn, and $N_{ind}$ is the number of independent nodes.

The solution to the stream functions is given as:

$$\boldsymbol{\Phi_i^0} = -\boldsymbol{H}^{-1}\,\boldsymbol{Z_{ii'}^{-1}}\,\boldsymbol{Z_{ib}}\,\boldsymbol{\Phi_b} \tag{16}$$

The vector $\boldsymbol{\Phi_i}$ is calculated from equations (15,16). Similar to the solid track, $\boldsymbol{\Phi_i}$ and $\boldsymbol{\Phi_b}$ for a turn are concatenated to create the vector $\boldsymbol{\Phi}$. And per turn resistance and the inductance are calculated as in equations (13, 14).

A computational framework from the above equations is implemented on MATLAB® (MathWorks, MA). Meshing the coils' tracks and computing the parameters of the triangular elements is achieved by an implemented mesher in MATLAB. Some of the simulations in this work are verified by Ansys Maxwell (Ansys, Inc., PA). Both MATLAB and Ansys ran on an Intel (R) Core (TM) i7 CPU (2.60 GHz) laptop with 16 GB RAM. It is noted that the stream function equations (12 and 16) were solved in MATLAB using the backslash operator for computational robustness.

### A. SINGLE TURN LOOP AND GOLAY COIL

A simulation is done by the implemented framework to demonstrate the current distribution on a single turn loop with finite track width to show how the current density and resultant magnetic fields are affected by track widths. The turn is 10 cm radius, 0.1 to 40 mm in width, and 2 mm in thickness. The turn track is meshed into sections of 1mm width that are meshed into triangles with a maximum segment length of 10 mm in the circumferential direction. The 1mm wide coil is meshed into 3 sub-tracks. The material of the turn is copper with a resistivity of $1.7\times10^{-8}$ Ωm. A current of 100 A passes through the turn by setting the stream functions of the boundary nodes as discussed previously. The simulation is done for selected excitation frequencies from 10 Hz up to 10 kHz.

The current density on the turn track, the resistance, and the inductance of the turn at different frequencies are calculated via the framework and also compared with Ansys results of the same turn configuration. For more validation, DC resistance and inductance of the turn are compared with closed-form in [31] and [32].

The resultant gradient field for a Golay coil [33] of different track widths (1 to 7 cm) is compared. The radius of the Golay coil is set to 10 cm while the current is 100 A. The Golay's track is meshed similarly to the single loop.

### B. GRADIENT COIL DESIGN AND OPTIMIZATION

For validation, self-shielded Z gradient (longitudinal) and X gradient (transverse) coils of specific track width are designed in this work (comparable to previously published coil designs [5], [28]). The radius and the length of primary and shielding coils of the Z gradient differ from those of the X gradient as will be discussed in the next subsections. In both gradient coils, the DSV is 50 cm. The radius and the length of the cryostat cylinder are 43 cm, and 146 cm, respectively.

#### 1) GRADIENT COIL PARAMETERS

For all the gradient coil turns, the current densities in the triangular elements on all turns are calculated. The magnetic field from these currents on the DSV ($B_z$ component) and the cryostat cylinder ($B_x$, $B_y$, and $B_z$ components) are calculated using Biot-Savart law [17], [18], [19] in terms of volume currents as follows:

$$\vec{B} = \frac{\mu_0}{4\pi}\iiint_V \frac{\left(\vec{J}dv\right)\times\overrightarrow{r'}}{\left|\vec{r}'^3\right|} \tag{17}$$

where $v$ is the track elements volume, and $\overrightarrow{r'}$ is the vector from the triangular elements on the coil tracks to the target points.

The following parameters are used as design metrics for coil optimization and performance evaluation [5], [6], [28]:

1) The average gradient strength ($G_m$) over the DSV:

$$G_m = \frac{1}{M}\sum_{i=1}^{M} G_i \tag{18}$$

where $G_i$ is the gradient strength and $M$ is the overall number of points on the DSV.

2) The coil efficiency ($\eta$) :

$$\eta = \frac{G_m}{I} \tag{19}$$

where $I$ is the current that passes in the gradient coil.

3) The linearity error ($LinE$):

$$LinE = \frac{G_{max} - G_{min}}{G_{max} + G_{min}} \times 2 \times 100\% \tag{20}$$

where $G_{min}$ and $G_{max}$ are the minimum and the maximum gradient strength at the DSV points.

4) The figure of power (*FoP*):

$$FoP = \frac{\eta^2}{R} \tag{21}$$

where R is the resistance of the coil.

5) The average shielding ratio (*SHRa*) at the cryostat:

$$SHRa = \left(1 - \frac{avg\left(\left|\vec{\boldsymbol{B}}_{pri} + \vec{\boldsymbol{B}}_{sh}\right|\right)}{avg\left(\left|\vec{\boldsymbol{B}}_{\boldsymbol{pri}}\right|\right)}\right) \times 100 \tag{22}$$

where $\vec{\boldsymbol{B}}_{\boldsymbol{pri}}$ and $\vec{\boldsymbol{B}}_{\boldsymbol{sh}}$ are the magnetic field vectors at the presumed points on the cryostat created by the primary and shielding coils, respectively.

### 2) Z GRADIENT COIL

Four groups of coaxial circular turns are distributed on two separated concentric cylinders (primary and shielding) with radiuses of $r_p$ and $r_s$. On each cylinder, the turns are symmetrically located at the $+z$ side and $-z$ side. The turns' locations extend from 0 to $\pm z_{l/2}$ ($z_{l/2}$ is the half-length of the cylinder). The coordinates of the turns of the primary or shielding coil as a function of a radius can be expressed as:

$$\begin{aligned} x &= r\cos(\theta) \\ y &= r\sin(\theta) \\ z &= \pm z_i \end{aligned} \tag{23}$$

where $(0 \leq \theta \leq 2\pi)$, $z_i$ is a turn location, $i = 1, 2, \ldots, N$, and N is the number of turns on one cylinder side. A constraint on the distance between any two consecutive turns is given as $|z_{i+1} - z_i| > d$.

The radii of primary and shielding cylinders are 330 mm and 380 mm respectively. And the lengths of the cylinders are 1246 mm and 1286 mm respectively similar to [5]. The width of the turn track is set to 10 mm while the thickness is set to 2 mm. The minimum distance between any consecutive turns $d$ is 12 mm. The turn track in the circumferential direction is discretized into segments of 30 mm. The track in the width direction is meshed into nine sections of single-layer structured triangular elements.

The locations of the turns on the primary and shielding cylinders are optimized by *fmincon* MATLAB® function where its purpose is to minimize the multi-objective function:

$$\begin{aligned} f(x) = {} & \alpha_1\, norm\left[LinE(x)\right] + \alpha_2\, norm\left[SHRa(x)\right] \\ & + \alpha_3\, norm\left[G_m(x)\right] \end{aligned} \tag{24}$$

where $x$ is a vector that represents the locations of the turns. The weighting factors $\alpha_1$, $\alpha_2$, and $\alpha_3$ were set, in this work, to 1/3 where equal priority is given to each optimization term. To avoid scaling issues, the objective parameters were normalized according to [34] where $norm[f(x)] = |f(x) - target([f(x)])|/target[f(x)]$.

The target of the parameters *LinE*, *SHRa*, and *Gm* were set to 5%, 95%, and 45 mT/m, respectively. In both the primary and shielding coils, the locations of the turns are symmetric in z-direction in both halves of the cylinder. The optimization of the turns' location is done only for onehalf of the cylinder. The upper and lower bounds of the turns' location were set between 0-1246/2 mm and 0-1286/2 mm for the primary coil and the shielding coil respectively. Linear inequality constraints were set to the distance between the consecutive turns ( $Ax \leq b$ in *fmincon)*

After achieving the final Z gradient coil, the whole coil performance is calculated for the solid, slitted tracks as well as for the thin wire coil.

In the slitted track Z gradient coil configuration, the track of 10 mm is slitted into three sub-tracks by two slits of 1mm width. Each sub-track is divided into three sections of structured triangular elements

### 3) X GRADIENT COIL

The turns are presumed to have a quasi-elliptical shape which is mathematically represented as in [5] and [6]. Similar to the approach followed in [28], the turn track width is set to around 5 mm while its thickness is set to 2 mm. Because of the curvature of the coil turn, the turn track width varies between 5-5.5 mm. Similar to the Z gradient coil, the X gradient turns' tracks are meshed into a singular layer of structured triangular elements. The coil turn in the circumferential direction is discretized into segments of 20 mm while in the track's width direction is meshed into five sections of structured triangular elements. The radius and the length for the primary cylinder are 320 mm and 1286 mm respectively, while they are 370 mm and 1326 mm for the shielding cylinder similar to [5].

Both the primary and the shielding cylinders have four symmetric quadrants. The number of the primary coil turns is searched over 18-23 turns for one quadrant. All the turns have the same center. In the searching process, the primary turns are moved so they occupy 24 possible locations and their center can be located at 50 available locations. The magnetic field over the DSV from the all-possible combinations of primary turns as well as their total resistance are calculated. The elected number for the primary coil has the best FoP with LinE $< 10\%$. Only the combinations containing the elected number of turns with linE$<10\%$ are saved as candidate primary locations for the next process which involves shielding turns to elect the optimal whole gradient coil.

For the shielding coil, the number of turns is searched over 10-16 turns (for one quadrant) which occupy 22 possible locations and their center can move over 100 locations. Using brute-force search, the whole gradient coil is searched over the candidate's primary combinations with shielding combinations to get the final whole gradient coil which has the best FoP and is constrained by LinE $< 9\%$ and SHRa $> 85\%$. Fig.4 shows the possible locations which can be occupied by shielding turns and their center can move up or down (indicated by the red arrow) over 100 locations. Fig.5 illustrates a flow chart of the algorithm used to optimize the whole self-shielded X gradient coil by brute-force search.

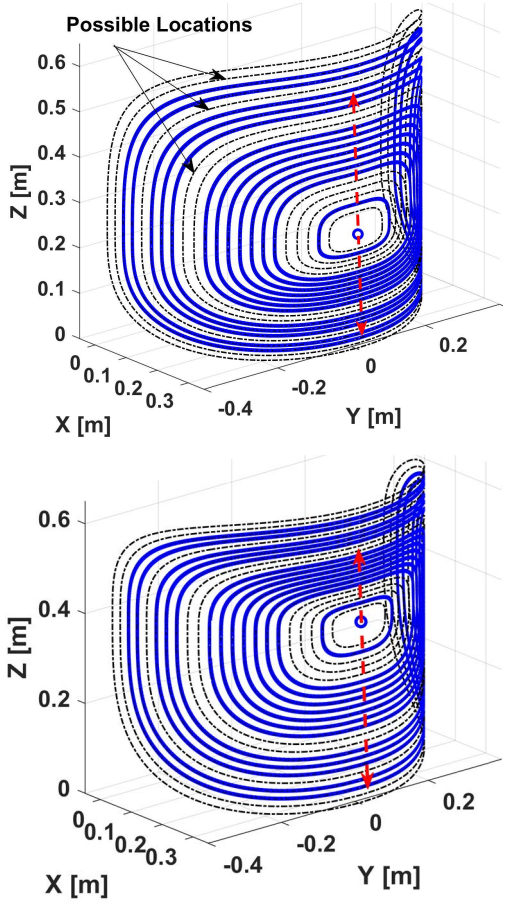


**FIGURE 4.** An illustration for a quadrant of shielding coil of 13 turns to occupy 22 possible locations. The coils' center moves up-down 100 locations along the search line.

### C. FREQUENCY EFFECT ON RESISTANCE AND INDUCTANCE

Skin effect has an influence on the effective cross-section of the coil track and that is accompanied by a change in both the resistance and inductance of the coil [35], [36]. The frequency-dependent resistances and inductances of the final designed Z and X gradient coils are studied using the implemented framework. The gradient coils' turns are separated so the connections between them are ignored in the simulations. Both solid and slitted track coils' configurations are considered for the Z gradient. The simulations are done with a current source at the selected frequencies from 0 Hz to 10 kHz.

For the entire coil, the resistance matrix $\mathcal{R}$, the inductance matrix $\mathcal{M}$ and the impedance matrix $\mathbb{Z}$ are constructed due to the interaction of the pair of nodes $n$ and $m$ on all the turns of the gradient coil. The stream functions $\mathbf{\Phi}$ for the whole gradient coil is a concatenation of the boundary nodes $\mathbf{\Phi_b}$ and the internal nodes $\mathbf{\Phi_i}$ of all turns. The stream functions of the internal nodes are computed similarly to equation (12). At a specific frequency, the resistance and inductance of the whole gradient coil are calculated using equations (12-14).

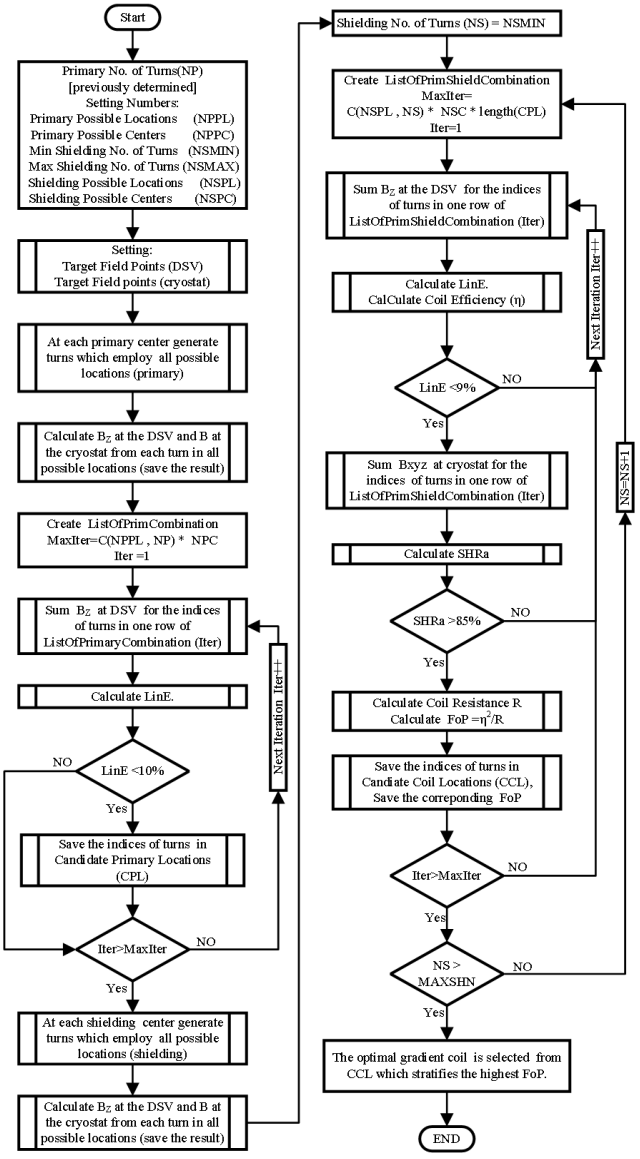


**FIGURE 5.** The flowchart of X gradient coil optimization.

### D. HARMONICS AND TRANSIENT EDDY CURRENTS ANALYSES

The switching of the gradient field by a gradient coil induces eddy currents in the surrounding conducting material such as the cryostat, the passive shield, the passive gradient coils, etc. [31], [37], [38], [39], [40], [41]. Due to the closeness of gradient coils to each other, the eddy currents induced in the close passive coils are expected to be greater than those induced in the further metallic structures such as the cryostat.

Considering the coil with tracks makes it possible to study the interaction between the gradient coils. Via the implemented framework, the harmonics and transient eddy currents interaction are studied between the designed X and Z gradient coil. In both harmonic and transient interaction analysis, the X gradient coil is activated while the Z gradient coil is set non-active (passive). Two configurations of Z gradient coil are included in the analysis: the solid tracks, and the slitted

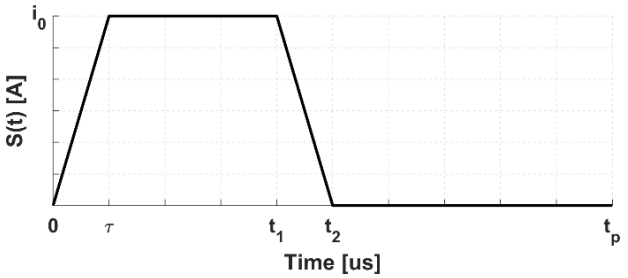


**FIGURE 6.** A typical trapezoidal current pulse.

tracks. To reduce the computation, the track of the X gradient coil in the width direction is meshed into one section, while the Z gradient coil is meshed into nine sections of structured triangular elements

To calculate the eddy current dissipated power in the passive Z gradient (harmonic analysis), the X gradient coil is activated by a current of 600 A of frequency 1kHz. The harmonics solution is obtained similar to equation (12) where the nodes on all the turns' tracks for both X and Z gradient coils are included in the formulations (4-12).

The AC power loss $P$ (in Watt) due to the induced eddy currents on the passive Z gradient can be given in terms of volume eddy currents density as [42], [43]:

$$P = \frac{1}{2}\iiint_V \frac{\vec{J}\cdot\overrightarrow{J^*}}{\sigma}\,dv \tag{25}$$

where $dv$ is the volume element, $\sigma$ is the conductivity of the coils' material, and $*$ denotes the complex conjugate. The power dissipation (in dBm) due to the eddy currents is calculated from the power loss as [44]:

$$\text{Power dissipation (dBm)} = 10\log\left(\frac{P}{1\text{mW}}\right) \tag{26}$$

For the transient analysis, the X gradient excitation current is assumed to have a trapezoidal waveform. The boundary nodes' stream functions $\mathbf{\Phi_b}$ at one side of each turn of the X gradient coil are properly set to zeros while at the other side of the turn are set as $S(t)$ function as follows:

$$S(t) = \begin{cases} \dfrac{i_0 t}{\tau} & 0 \le t \le \tau \\ i_0 & \tau < t \le t_1 \\ \dfrac{-i_0\,(t-t_2)}{\tau} & t_1 < t \le t_2 \\ 0 & t_2 < t \le t_p \end{cases} \tag{27}$$

where $\tau$ is the ramp-up and ramp-down times as depicted in Fig.6, $i_0$ is the pulse current amplitude, and $t_p$ is repetition time. The trapezoidal current is set with equal ramp-up and ramp-down times of 200 *us*, flat-top time 600 *us*, the repetition time 2000 *us*, and the amplitude of the current ($i_0$) 600 A.

Similar to the temporal circuit equation (5), the parameters are constructed by involving the nodes on all the turns' tracks for both X and Z gradient coils. The parameters in the equation are broken down to an internal, boundary, and a combination of internal/boundary sections, and the final equation is rewritten as:

$$\begin{bmatrix} \mathcal{R}_{\mathbf{bb}} & \mathcal{R}^{\mathbf{T}}_{\mathbf{ib}} \\ \mathcal{R}_{\mathbf{ib}} & \mathcal{R}_{\mathbf{ii}} \end{bmatrix}\begin{bmatrix} \mathbf{\Phi_b} \\ \mathbf{\Phi_i} \end{bmatrix} + \begin{bmatrix} \mathcal{M}_{\mathbf{bb}} & \mathcal{M}^{\mathbf{T}}_{\mathbf{ib}} \\ \mathcal{M}_{\mathbf{ib}} & \mathcal{M}_{\mathbf{ii}} \end{bmatrix}\frac{1}{\partial t}\begin{bmatrix} \mathbf{\Phi_b} \\ \mathbf{\Phi_i} \end{bmatrix} = \begin{bmatrix} 0 \\ 0 \end{bmatrix} \tag{28}$$

The following differential equation gives the temporal solution to the internal nodes stream functions $\mathbf{\Phi_i}\,(t)$:

$$\frac{\partial \mathbf{\Phi_i}}{\partial t} + \mathcal{M}^{-1}_{\mathbf{ii}}\mathcal{R}_{\mathbf{ii}}\mathbf{\Phi_i} = -\mathcal{M}^{-1}_{\mathbf{ii}}\mathcal{R}_{\mathbf{ib}}\mathbf{\Phi_b} - \mathcal{M}^{-1}_{\mathbf{ii}}\mathcal{M}_{\mathbf{ib}}\frac{\partial \mathbf{\Phi_b}}{\partial t} \tag{29}$$

Let

$$W = \mathcal{M}^{-1}_{\mathbf{ii}}\mathcal{R}_{\mathbf{ii}}$$

where $\mathcal{M}_{\mathbf{ii}}, \mathcal{R}_{\mathbf{ii}}$ are the inductance and resistance matrices associated with the internal/internal nodes. $\mathcal{M}_{\mathbf{ib}}, \mathcal{R}_{\mathbf{ib}}$ are the inductance and the resistance matrices associated with the internal and the boundary nodes, and $\mathcal{M}_{\mathbf{bb}}, \mathcal{R}_{\mathbf{bb}}$ are the inductance and resistance matrices associated with the boundary/boundary nodes. By diagonalizing the matrix $\boldsymbol{W}$, we can write:

$$\mathbf{D} = \mathbf{U}^{-1}\mathbf{W}\,\mathbf{U}$$

$$\mathbf{D} = \begin{bmatrix} \lambda_1 & \cdots & 0 \\ \vdots & \ddots & \vdots \\ 0 & \cdots & \lambda_k \end{bmatrix}$$

where $\mathbf{U}$ is a matrix contains the eigenvectors of the matrix $\mathbf{W}$, $\mathbf{D}$ is a diagonal matrix whose diagonal elements are the eigenvalues $(\lambda_1, \ldots, \lambda_k)$ of the matrix $\mathbf{W}$, and $k$ is the number of internal nodes. The general temporal solution to the above first-order differential equation (29) is given as:

$$\begin{aligned} \mathbf{\Phi_i}\,(\mathbf{t}) = \mathbf{U}\Bigg[ & \mathbf{\Phi_i}\,(\mathrm{t_0})\,\mathbf{e}^{\boldsymbol{\lambda}(\mathrm{t_0}-\mathrm{t})} \\ & - \mathbf{e}^{-\boldsymbol{\lambda} t}\left[\int_{\mathrm{t_0}}^{\mathrm{t}} \mathbf{e}^{\boldsymbol{\lambda}\zeta}\mathbf{U}^{-1}\mathbf{M}^{-1}_{\mathbf{ii}}\mathbf{R}_{\mathbf{ib}}\mathbf{\Phi_b}\,(\zeta)\,\mathrm{d}\zeta\right. \\ & \left. + \int_{\mathrm{t_0}}^{\mathrm{t}} \mathbf{e}^{\boldsymbol{\lambda}\zeta}\mathbf{U}^{-1}\mathbf{M}^{-1}_{\mathbf{ii}}\mathbf{M}_{\mathbf{ib}}\frac{\partial \mathbf{\Phi_b}\,(\zeta)}{\partial \zeta}\mathrm{d}\zeta\right]\Bigg] \end{aligned} \tag{30}$$

where $\mathrm{t_0}$ is the initial time, $\boldsymbol{\lambda}$ is the eigenvalues vector $[\lambda_1 \ldots \lambda_k]$, and $\zeta$ is a dummy variable.

The calculated $\mathbf{\Phi_i}$ and $\mathbf{\Phi_b}$ are concatenated to create the vector $\mathbf{\Phi}$. The current densities in the triangular elements on the tracks of the active coil (X gradient) and passive coil (Z gradient) are calculated as in equation (4). The net magnetic field from the two coils is calculated on a target point inside the coils. An appropriate boundary condition is set to prevent the excitation current and the induced eddy currents from crossing the edge of the tracks where equation (15) is involved in the above formulations. We preferred to

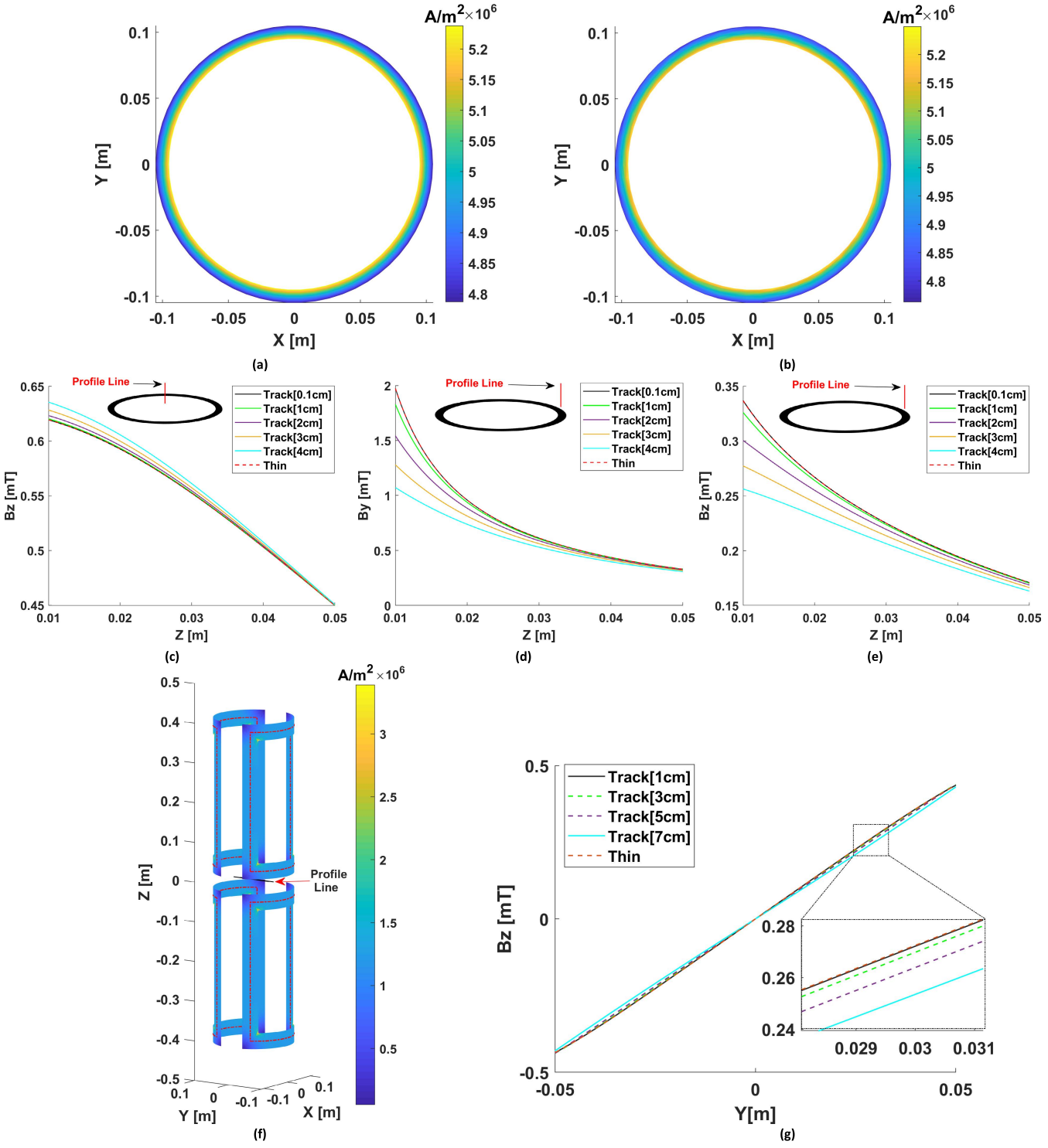


**FIGURE 7.** The current densities distribution on the track of the single circular turn of 1 cm width is computed by Ansys (a) and our computational framework (b). The magnetic field components for different track widths of the single circular turn at the red profile lines extend from (0,0,1) cm to (0,0,5) cm (c), and from (0,10,1) cm to (0,10,5) cm (d and e) are plotted in comparison to the thin wire assumption. The current densities distribution on the track of Golay's coil with a track width of 4 cm is computed (f). The center line of the Golay coil is shown by red dotted lines. The resultant $B_z$ magnetic field of the Golay coil for several track widths are plotted for the black profile line extending from (0, −5,0) cm to (0,5,0) cm (g). A zoom in for the magnetic fields of the profile line is also illustrated.

use this direct formulation to avoid the challenging problem of determining the appropriate time step when time stepping methods are employed [45], [46] that affects the stability and accuracy of the solution. Despite that equation (30) initially involves relatively expensive computations of matrix inversions followed by diagonalization; however, this is only

**TABLE 1. The resistance (R) and inductance (L) of the single turn are calculated by the framework (FW) and ansys (ANS) at different frequencies.**

| | 10 Hz | 100 Hz | 1 kHz | 10 kHz |
|---|---|---|---|---|
| L (nH) ANS | 465.67 | 465.64 | 463.71 | 452.25 |
| L (nH) FW | 484.58 | 484.54 | 481.55 | 472.27 |
| R ($\mu\Omega$) ANS | 533.66 | 534.02 | 563.24 | 947.57 |
| R ($\mu\Omega$) FW | 533.75 | 534.23 | 569.73 | 993.56 |

performed once for the system matrices. Since the shape of the pulse is predefined, this allows a direct numerical solution for the transient problem as previously shown in [31].

## III. RESULTS AND DISCUSSION

### A. SINGLE TURN LOOP AND GOLAY COIL

The computed current densities $Am^{-2}$ from the framework and Ansys is plotted for the single turn, Fig.7 (a). The Ansys result, Fig.7 (b), partially verifies the core of our computational framework where it is obvious that the two current distributions are comparable. The current distribution on the turn is not uniform and it depends on the geometry of the turn. The inner side of the turn track has more current density than the outer side.

The resistance and inductance of the turn are computed via our computational framework and Ansys at selected frequencies as tabulated in TABLE 1. The result of the framework agreed with Ansys within an error range of 0.02-4.9% for the resistance and 3.8-4.4% for the inductance. Analytical DC calculations of the resistance and inductance of the turn using the closed forms in [31] give extra verification for the framework. The DC (i.e., at 0 Hz) values of both the resistance and inductance of the turn are 533.743 m$\Omega$ and 484.5845 $\mu H$, respectively, which agree with the values calculated by the closed forms with errors of 0.06% and 0.7%, respectively.

For all selected frequencies in TABLE 1, the implemented framework takes a few seconds to compute the resistance, inductance, as well as current density distribution on the turn while Ansys takes approx. 30 minutes to achieve the same tasks. The accuracy and the efficiency of the framework are thus tested for a single loop.

The skin depth of the copper at 1 kHz is approx. 2.1 mm which is approx. equal to the thickness of the turn. For frequencies less than 1 kHz, the current is uniform at the turn cross-section and the frequency does not affect the turn resistance. For higher frequencies $\gg$ 1 kHz, the skin depth of the turn is smaller than the turn thickness and the current at the turn cross-section cannot be considered uniform any longer. This skin depth effect of current has a great influence on the resistance of the turn especially at the high frequencies and that should be taken into account in the resistance computation. The resistance is compensated as suggested in [22], [47] by multiplying the resistance matrix by a compensation factor which is a function of the turn thickness and the skin depth.

**TABLE 2. The designed Z gradient coil performance parameters.**

| PARAMETERS | SOLID WIDE TRACK WIRE | SLITTED WIDE TRACK WIRE | THIN WIRE |
|---|---|---|---|
| Efficiency $\eta$ ($Tm^{-1}A^{-1}$) | $6.96 \times 10^{-05}$ | $6.96 \times 10^{-05}$ | $7.01 \times 10^{-05}$ |
| Inductance L ($\mu$H) | 464.59 | 466.22 | --- |
| Resistance (m $\Omega$ ) | 193.97 | 242.47 | 193.73 |
| FoM $\eta^2/L$ ($T^2m^{-2}A^{-2}H^{-1}$) | $1.04 \times 10^{-05}$ | $1.04 \times 10^{-05}$ | --- |
| FoP $\eta^2/R$ ($T^2m^{-2}A^{-2}\Omega^{-1}$) | $2.5 \times 10^{-08}$ | $2 \times 10^{-08}$ | $2.54 \times 10^{-08}$ |
| No of turns P/S | 32/20 | 32/20 | 32/20 |
| Lin error at DSV=50cm | 5.95 | 5.96 | 5.87 |
| Lin error at DSV=45cm | 3.98 | 3.98 | 3.84 |
| Lin error at DSV=40cm | 2.70 | 2.70 | 2.57 |
| SHRa (%) | 92.92 | 92.91 | 92.58 |
| $\|B\|_{max}$(Gauss) at the cryostat (I=600A) | 17.33 | 17.33 | 16.99 |
| $\|B\|_{mean}$(Gauss) at the cryostat (I=600A) | 6.78 | 6.79 | 7.05 |
| $G_z$ (mT/m) at I=600A | 41.78 | 41.79 | 42.09 |

T = Tesla, m = meter, A = Ampere, H = Henry, $\Omega$= Ohm
Note: the performance metrics are computed utilizing the distributed points used for the coil design (400 for DSV and 400 for the cryostat)

Fig.7 (c, d, and e), show the magnetic fields on two profile lines at the center and the edge of the circular turn for different track widths versus the thin wire coil. For the centered profile line, $B_z$ component is only plotted where $B_x$ and $B_y$ components are zeros. For the edge profile line, $B_y$ and $B_z$ are plotted while $B_x$ is zero. It is obvious from the plots that when the track width is very small (close to the thin wire), the resultant magnetic fields are identical to those induced by the thin wire. When the track width of the coil increases, a significant difference in the magnetic fields is noticed.

Similarly, the current density distribution on the Golay's coil track is computed as shown in Fig.7 (f). The magnetic field $B_z$ of the Golay's coil for several track widths as well as the thin wire are displayed on Fig.7 (g). The magnetic fields $B_x$ and $B_y$ are not included because they are equal to zero. Again, the resultant gradient fields for Golay's coil of wide tracks differ from the thin wire assumption.

### B. GRADIENT COIL DESIGN AND OPTIMIZATION

The optimized Z and X gradient coils are illustrated as 3D plots in Fig.8 (a) and Fig.8 (b), respectively. They are demonstrated together in the same 3D plot in Fig.8 (c). The transverse view and the coronal section view are also illustrated in Fig.8 (d) and Fig.8 (e), respectively. The colors on the plots indicate the direction of the currents on the turns.

The DC performances of the Z and X gradient coils are tabulated in TABLE 2 and TABLE 3, respectively. The performances of three different configurations of the Z gradient coil

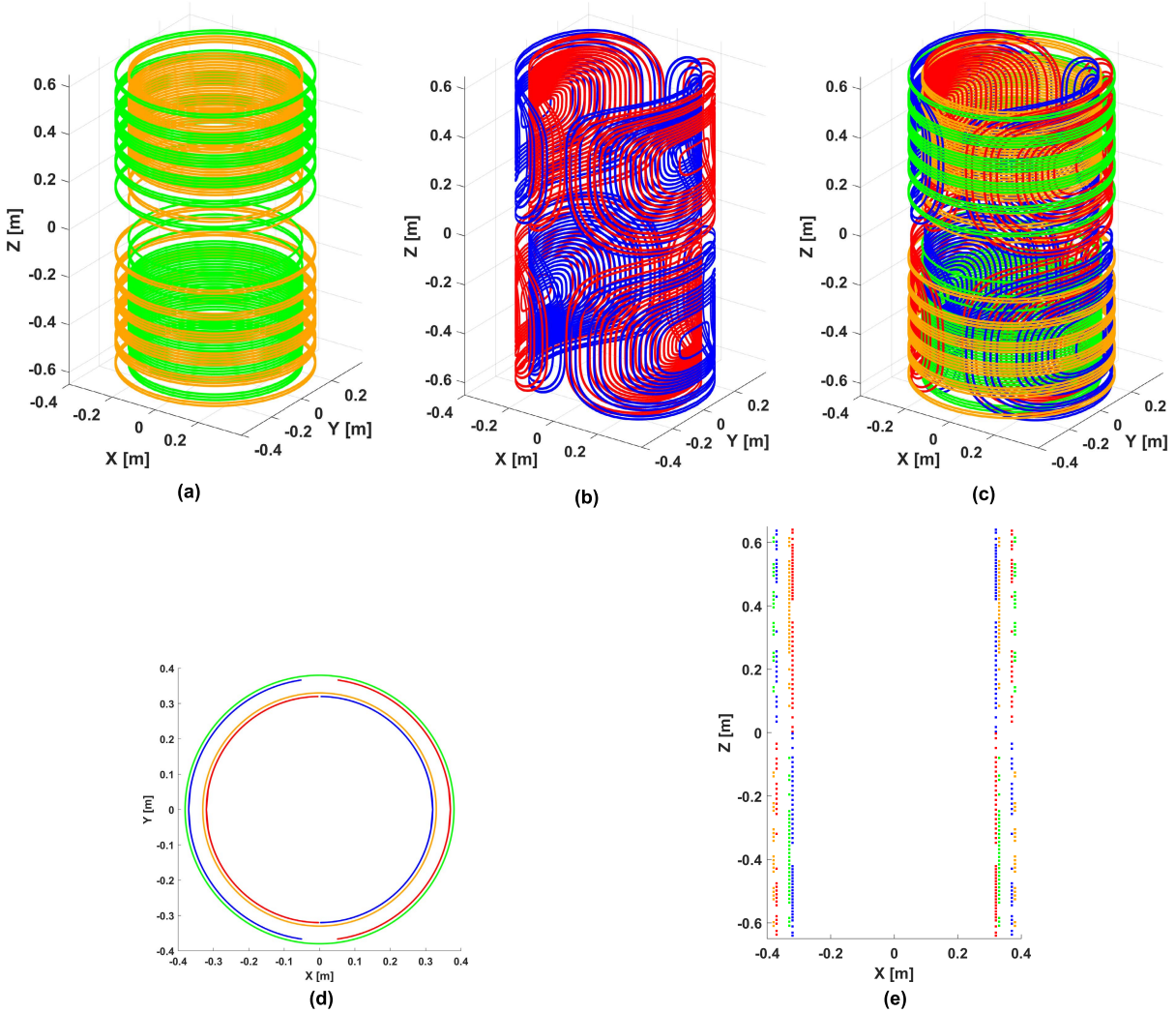


**FIGURE 8.** A 3D plot of the designed self-shielded Z gradient coil (a) and the designed self-shielded X gradient coil (b). The Z and X gradient coils in one 3D plot (c) and their transverse view (d) and coronal section view (e). Different Colors in the same coil indicate the direction of the current.

are computed and included in TABLE 2: solid track, slitted track, and thin wire. A noticeable difference in the resistance of the coil between the solid and slitted track configurations is observed. However, a slight increase in the inductance of the coil is noticed. The presence of the slits on the tracks of the coil decreases the effective cross-section of the track and that explains the reason for the increase in the resistance and inductance of the coil.

The DC performances of the gradient coils of wide track and thin wire configurations are approximately similar because the track widths used are not that wide and that validates the approach presented in this work. Although, the thin wire assumption for coil design is less computationally intensive but it is not general and can result in inaccuracies even for thin tracks as exemplified in the shielding ratio calculation for the designed transverse coil (we attribute this to the closeness of the field calculations to the tracks and the transverse coil geometry). Obviously, this is expected to be exacerbated for wider tracks. Considering coil track widths allows direct computation of the resistance and inductance of the coil. The FoP and FoM characteristics, in terms of resistance and inductance, respectively, are comparable to the previously published coil designs of similar dimensions in [5].

It is also worth noting that the linearity error for DSVs $\leq 50$ cm is $< 5\%$ as preferable for effective MRI. The linearity of the gradient field ($B_z$) of the designed gradient coils are illustrated on different planes inside the DSV as shown in Fig.9.

### C. FREQUENCY EFFECT ON RESISTANCE AND INDUCTANCE

Frequency has a noticeable effect on the resistance and a slight effect on the inductance of the coil as shown in TABLE 4. As the frequency increases, the resistance of the coil increases noticeably due to the reduction of the effective cross-section of the coil.

**TABLE 3.** The designed X gradient coil performance parameters.

| PARAMETERS | WIDE TRACK WIRE | THIN-WIRE |
|---|---|---|
| Efficiency η ($Tm^{-1}A^{-1}$) | 5.55 x$10^{-5}$ | 5.57 x$10^{-5}$ |
| Inductance L (μH) | 389.653 | --- |
| Resistance R (mΩ ) | 365.8923 | 380.08 |
| FoM $\eta^2/L$ ($T^2m^{-2}$ $A^{-2}H^{-1}$) | 7.92x$10^{-6}$ | --- |
| FoP $\eta^2/R$ ($T^2m^{-2}$ $A^{-2}\Omega^{-1}$) | 8.43x$10^{-9}$ | 8.17 x$10^{-9}$ |
| No of turns P/S | 22/13 | 22/13 |
| LinE at the DSV=50cm (%) | 8.31 | 9.45 |
| LinE at the DSV=45cm (%) | 5.28 | 6.1 |
| LinE at the DSV=40cm (%) | 3.34 | 3.97 |
| SHRa (%) | 85.07 | 82.45 |
| $\|B\|_{max}$ (Gauss) at the cryostat (I=600A) | 27.656 | 27.504 |
| $\|B\|_{mean}$ (Gauss) at the cryostat (I=600A) | 12.9728 | 12.9018 |
| $G_x$ (mT/m) at I=600A over DSV=50cm | 33.33 | 33.43 |

T = Tesla, m = meter, A = Ampere, H = Henry, Ω= Ohm
Note: the performance metrics are computed utilizing the distributed points used for the coil design (199 for DSV and 132 for the cryostat)

**TABLE 4.** Effect of frequency on the resistance and inductance of the gradient coils.

| | 0 Hz | 10 Hz | 100 Hz | 1 kHz | 10 kHz |
|---|---|---|---|---|---|
| ZL Solid (μH) | 464.5916 | 464.5913 | 464.5627 | 462.5527 | 456.3303 |
| ZL Slitted (μH) | 466.2242 | 466.2245 | 466.1989 | 464.4239 | 460.0573 |
| ZR Solid (mΩ) | 193.9743 | 193.9775 | 194.2884 | 217.3073 | 426.4143 |
| ZR Slitted (mΩ) | 242.4685 | 242.4711 | 242.7332 | 261.5909 | 430.1443 |
| XL Solid (μH) | 389.653 | 389.653 | 389.649 | 389.299 | 385.9695 |
| XR Solid (mΩ) | 365.9019 | 365.9029 | 366.003 | 375.2391 | 633.1313 |

Z: z-gradient, X:x-gradient, R: Resistance, L: Inductance

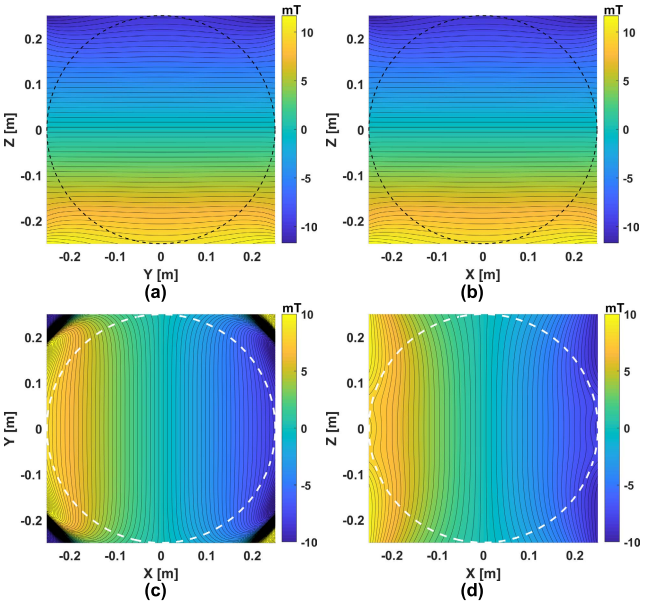


**FIGURE 9.** The magnetic fields $B_z$ on X=0 plane (a) and Y=0 plane (b) are produced by the Z gradient coil. The magnetic fields $B_z$ on the transverse plane at Z=0 (c) and Y=0 plane (d) are produced by the X gradient coil. The fields' linear dependency on the Z and X locations are illustrated inside a DSV of 50 cm.

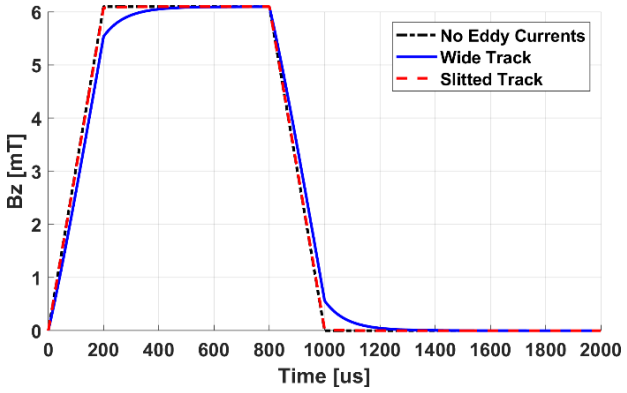


**FIGURE 10.** The temporal magnetic field $B_z$ is produced by the active X gradient and passive Z gradient at an arbitrary point P(315,0,300) mm inside the coils with three configurations: Z gradient of wide track, Z gradient of slitted track, and no eddy currents.

The reasons for the slight decrement of inductance with increasing the frequency are discussed in detail in [35]. As previously discussed in the single turn simulation, slitting affects the resistance and inductance of the coil where both of them increase at different levels with the existence of slits on the tracks.

### D. HARMONICS AND TRANSIENT EDDY CURRENTS ANALYSES

The harmonics eddy current analysis at 1kHz, shows the power dissipation on the Z gradient coil of solid tracks configuration is 64.03 dBm. However, it is 50.95 dBm on the slitted track configuration. Slitting has a significant contribution to the reduction of the eddy currents in the Z gradient coil. The electromagnetic interaction between the X and Z gradient coil is reduced by the presence of slits in the Z gradient tracks as suggested by [22].

In the transient eddy currents analysis, the magnetic field $B_z$ generated by the active X gradient coil and the passive Z gradient coil is calculated at an arbitrary point inside the coils. The magnetic fields $B_z$ are plotted versus the time corresponding to Z coil configurations and no eddy currents case as shown in Fig10. The transient eddy current effect is noticeable in the case of the solid track while it is almost not notable in the case of the slitted tracks and the thin wire. The eddy current induced on the solid Z gradient produces a secondary magnetic field that has a distortion effect on the magnetic field created by the X gradient specifically in the transient current locations.

## IV. CONCLUSION

We have developed a flexible computational framework for gradient coils design using finite track width. We have shown that using a single turn loop and a Golay coil, track width can potentially have an effect on computed magnetic fields particularly for wide tracks. This may generally depend on the relative dimensions of the gradient coil. Our design approach for a transverse and longitudinal gradient set having relatively small track widths was validated against thin wire computations where magnetic field computations have a minor effect on the computed coil's DC field-related performance parameters albeit for the shielding ratio for the transverse coil. In the future, wider track width can be considered using the same design approach.

Despite of that, considering the coil tracks as suggested in this work is still efficient for computing the frequency-dependent resistance and inductance which are required to calculate other coil performance parameters such as FoP and FoM. More importantly, with the presented framework, the harmonic and transient eddy current analysis of the intra-coil interaction is investigated which is not possible in the case of thin-wire assumption. Slitting the coil tracks affects both the resistance and inductance of the coil. The resistance significantly increases with the presence of slits with a slight increase in the inductance. Moreover, slitting contributes to the reduction of the intra-coil induced eddy currents. The demonstrated design framework is flexible to be adapted for further computations per design needs.

## REFERENCES

[1] S. A. Winkler, F. Schmitt, H. Landes, J. de Bever, T. Wade, A. Alejski, and B. K. Rutt, "Gradient and shim technologies for ultra high field MRI," *Neuroimage*, vol. 168, pp. 59–70, Mar. 2018.

[2] F. E. Elshahaby, B. A. Landman, and J. L. Prince, "Effect of regularization parameter and scan time on crossing fibers with constrained compressed sensing," *Proc. SPIE*, vol. 7962, Mar. 2011, Art. no. 79624J.

[3] S. S. Hidalgo-Tobon, "Theory of gradient coil design methods for magnetic resonance imaging," *Concepts Magn. Reson. A*, vol. 36, no. 4, pp. 223–242, 2010.

[4] R. Turner, "Gradient coil design: A review of methods," *Magn. Reson. Imag.*, vol. 11, no. 7, pp. 903–920, 1993.

[5] Y. Wang, X. Xin, F. Liu, and S. Crozier, "Spiral gradient coil design for use in cylindrical MRI systems," *IEEE Trans. Biomed. Eng.*, vol. 65, no. 4, pp. 911–920, Apr. 2018.

[6] X. Du, Z. Zhu, L. Zhao, G. Zhang, F. Ning, Z. Liu, Z. Hou, M. Wang, W. Ma, and W. Yao, "Design of cylindrical transverse gradient coil for 1.5 T MRI system," *IEEE Trans. Appl. Supercond.*, vol. 22, no. 3, Jun. 2011, Art. no. 4402004.

[7] S. Crozier, L. K. Forbes, and D. M. Doddrell, "The design of transverse gradient coils of restricted length by simulated annealing," *J. Magn. Reson. A*, vol. 107, no. 1, pp. 126–128, Mar. 1994.

[8] S. Crozier and D. M. Doddrell, "Gradient-coil design by stimulated annealing," *J. Magn. Reson. A*, vol. 103, no. 3, pp. 354–357, 1993.

[9] E. C. Wong, A. Jesmanowicz, and J. S. Hyde, "Coil optimization for MRI by conjugate gradient descent," *Magn. Reson. Med.*, vol. 21, no. 1, pp. 39–48, Sep. 1991.

[10] S. Zheng, X. Li, W. Q. Yan, and W. Xu, "Gradient coils design with regularization method for superconducting magnetic resonance imaging," in *Proc. Int. Conf. Image Vis. Comput. New Zealand (IVCNZ)*, Nov. 2018, pp. 1–5.

[11] Y. Wang, F. Liu, X. Zhou, and S. Crozier, "Design of transverse head gradient coils using a layer-sharing scheme," *J. Magn. Reson.*, vol. 278, pp. 88–95, May 2017.

[12] M. Zhu, L. Xia, F. Liu, J. Zhu, L. Kang, and S. Crozier, "A finite difference method for the design of gradient coils in MRI—An initial framework," *IEEE Trans. Biomed. Eng.*, vol. 59, no. 9, pp. 2412–2421, Sep. 2012.

[13] G. Shou, L. Xia, F. Liu, M. Zhu, Y. Li, and S. Crozier, "MRI coil design using boundary-element method with regularization technique: A numerical calculation study," *IEEE Trans. Magn.*, vol. 46, no. 4, pp. 1052–1059, Apr. 2010.

[14] H. S. Lopez, F. Liu, M. Poole, and S. Crozier, "Equivalent magnetization current method applied to the design of gradient coils for magnetic resonance imaging," *IEEE Trans. Magn.*, vol. 45, no. 2, pp. 767–775, Feb. 2009.

[15] M. Poole and R. Bowtell, "Novel gradient coils designed using a boundary element method," *Concepts Magn. Reson. B, Magn. Reson. Eng., Educ. J.*, vol. 31, no. 3, pp. 162–175, Aug. 2007.

[16] R. Turner, "A target field approach to optimal coil design," *J. Phys. D, Appl. Phys.*, vol. 19, no. 8, pp. L147–L151, Aug. 1986.

[17] I. S. Grant and W. R. Phillips, *Electromagnetism*. Hoboken, NJ, USA: Wiley, 2013.

[18] D. J. Griffiths, *Introduction to Electrodynamics*. College Park, ND, USA: American Association of Physics Teachers, 2005.

[19] J. D. Jackson, *Classical Electrodynamics*. College Park, ND, USA: American Association of Physics Teachers, 1999.

[20] P. T. While, J. G. Korvink, N. J. Shah, and M. S. Poole, "Theoretical design of gradient coils with minimum power dissipation: Accounting for the discretization of current density into coil windings," *J. Magn. Reson.*, vol. 235, pp. 85–94, Oct. 2013.

[21] N. B. Roozen, P. P. H. Philips, D. Biloen, P. Limpens, and H. H. Tuithof, "Active vibration isolation applied to a magnetic resonance imaging (MRI) system," in *Proc. 12th Int. Congr. Sound Vib. (ICSV)*. Lisbon, Portugal: International Institute of Acoustics and Vibration, Jul. 2005.

[22] F. Tang, F. Freschi, H. S. Lopez, M. Repetto, F. Liu, and S. Crozier, "Intra-coil interactions in split gradient coils in a hybrid MRI–LINAC system," *J. Magn. Reson.*, vol. 265, pp. 52–58, Apr. 2016.

[23] F. Tang, F. Freschi, M. Repetto, Y. Li, F. Liu, and S. Crozier, "Mitigation of intra-coil eddy currents in split gradient coils in a hybrid MRI-LINAC system," *IEEE Trans. Biomed. Eng.*, vol. 64, no. 3, pp. 725–732, Mar. 2017.

[24] H.-S. Lopez, F. Freschi, A. Trakic, E. Smith, J. Herbert, M. Fuentes, S. Wilson, L. Liu, M. Repetto, and S. Crozier, "Multilayer integral method for simulation of eddy currents in thin volumes of arbitrary geometry produced by MRI gradient coils," *Magn. Reson. Med.*, vol. 71, no. 5, pp. 1912–1922, May 2014.

[25] F. Tang, H. S. Lopez, F. Freschi, E. Smith, Y. Li, M. Fuentes, F. Liu, M. Repetto, and S. Crozier, "Skin and proximity effects in the conductors of split gradient coils for a hybrid Linac-MRI scanner," *J. Magn. Reson.*, vol. 242, pp. 86–94, May 2014.

[26] R. A. Lemdiasov and R. Ludwig, "A stream function method for gradient coil design," *Concepts Magn. Reson. B, Magn. Reson. Eng., Educ. J.*, vol. 26, no. 1, pp. 67–80, 2005.

[27] A. Kameari, "Transient eddy current analysis on thin conductors with arbitrary connections and shapes," *J. Comput. Phys.*, vol. 42, no. 1, pp. 124–140, Jul. 1981.

[28] S. S. Alsharafi, A. M. Badawi, and A.-M. M. El-Sharkawy, "Design of a self-shielded transverse MRI gradient coil taking into account track width," Presented at the 5th IEEE MECBME, Amman, Jordan, Mar. 2020.

[29] S. S. Alsharafi, A. M. Badawi, and A.-M.-M. El-Sharkawy, "A comparative study for evaluating passive shielding of MRI longitudinal gradient coil," in *Proc. 43rd Annu. Int. Conf. IEEE Eng. Med. Biol. Soc. (EMBC)*, Nov. 2021, pp. 4444–4447.

[30] S. Adeeb, *Introduction to Solid Mechanics and Finite Element Analysis Using Mathematica*. Dubuque, IA, USA: Kendall Hunt, 2011.

[31] T. Kidane, W. Edelstein, T. Eagan, V. Taracila, T. Baig, Y.-C. Cheng, and R. Brown, "Active-passive shielding for MRI acoustic noise reduction: Network analysis," *IEEE Trans. Magn.*, vol. 42, no. 12, pp. 3854–3860, Dec. 2006.

[32] F. W. Grover, *Formulas and Tables for the Calculation of the Inductance of Coils of Polygonal Form*. Washington, DC, USA: U.S. Government Printing Office, 1923.

[33] R. Ansorge and M. Graves, *The Physics and Mathematics of MRI*. San Rafael, CA, USA: Morgan & Claypool, 2016.

[34] K. Deb, *Multi-Objective Optimization Using Evolutionary Algorithms*. Chichester, U.K.: Wiley, 2002.

[35] J. G. Coffin, *The Influence of Frequency Upon the Self-Inductance of Coils*, no. 37. Washington, DC, USA: U.S. Government Printing Office, 1906.

[36] A. Waygood, *An Introduction to Electrical Science*. Evanston, IL, USA: Routledge, 2013.

[37] W. A. Edelstein, T. K. Kidane, V. Taracila, T. N. Baig, T. P. Eagan, Y.-C.-N. Cheng, R. W. Brown, and J. A. Mallick, "Active-passive gradient shielding for MRI acoustic noise reduction," *Magn. Reson. Med.*, vol. 53, no. 5, pp. 1013–1017, 2005.
[38] A. Trakic, H. Wang, F. Liu, H. S. Lopez, and S. Crozier, "Analysis of transient eddy currents in MRI using a cylindrical FDTD method," *IEEE Trans. Appl. Supercond.*, vol. 16, no. 3, pp. 1924–1936, Sep. 2006.
[39] E. A. Badea and O. Craiu, "Eddy current effects in MRI superconducting magnets," *IEEE Trans. Magn.*, vol. 33, no. 2, pp. 1330–1333, Mar. 1997.
[40] H. S. Lopez, M. Poole, and S. Crozier, "Eddy current simulation in thick cylinders of finite length induced by coils of arbitrary geometry," *J. Magn. Reson.*, vol. 207, no. 2, pp. 251–261, Dec. 2010.
[41] H. Tsuboi, N. Seshima, I. Sebestyén, J. Pávó, S. Gyimóthy, and A. Gasparics, "Transient eddy current analysis of pulsed eddy current testing by finite element method," *IEEE Trans. Magn.*, vol. 40, no. 2, pp. 1330–1333, Mar. 2004.
[42] R. Bansal, *Handbook of Engineering Electromagnetics*. Boca Raton, FL, USA: CRC Press, 2004.
[43] J. R. Nagel, "Induced eddy currents in simple conductive geometries: Mathematical formalism describes the excitation of electrical eddy currents in a time-varying magnetic field," *IEEE Antennas Propag. Mag.*, vol. 60, no. 1, pp. 81–88, Feb. 2018.
[44] F. Costa, E. Laboure, and B. Revol, *Electromagnetic Compatibility in Power Electronics*. Hoboken, NJ, USA: Wiley, 2014.
[45] J. Dutiné, M. Clemens, S. Schöps, and G. Wimmer, "Explicit time integration of transient eddy current problems," *Int. J. Numer. Model., Electron. Netw., Devices Fields*, vol. 31, no. 2, p. e2227, Mar. 2018.
[46] J. C. Hardin, *ICASE/LaRC Workshop on Benchmark Problems in Computational Aeroacoustics (CAA)*. Washington, DC, USA: National Aeronautics and Space Administration, 1995.
[47] M. K. Kazimierczuk, *High-Frequency Magnetic Components*. Hoboken, NJ, USA: Wiley, 2011.

**SADEQ S ALSHARAFI** (Member, IEEE) received the B.Sc. and M.Sc. degrees from the Department of Systems and Biomedical Engineering, Faculty of Engineering, Cairo University, in 2006 and 2011, respectively, where he is currently pursuing the Ph.D. degree. He is currently a Lecturer at the Biomedical Technology Department, Sana'a Community College, Yemen. He has published around nine conference and journal publications as well as a book. His research interests include MRI gradient coil design, biomedical image processing, biomedical optics, and biomedical instrumentation.

**HAILE BAYE KASSAHUN** received the B.Sc. degree in electrical and computer engineering and the M.Sc. degree in biomedical engineering from Addis Ababa University, in 2013 and 2017, respectively. He is currently pursuing the Ph.D. degree with the Department of Systems and Biomedical Engineering, Cairo University. He worked as an Assistant Lecturer at the Center of Biomedical Engineering, Addis Ababa University, from 2014 to 2017. His research interests include MRI gradient coil design, medical physics, medical imaging, and biomedical image processing.

**AHMED M BADAWI** (Senior Member, IEEE) received the B.Sc., M.Sc., and Ph.D. degrees from the Department of Systems and Biomedical Engineering (SBME), Cairo University, Egypt, in 1990, 1993, and 1996, respectively. He was promoted to an Assistant Professor, an Associate Professor, and a Full Professor, in 1996, 2001, and 2007, respectively. He worked as a Visiting Professor at the Department of Biomedical Engineering, The University of Tennessee at Knoxville, Knoxville, TN, USA, from 2005 to 2007, and a Senior Research Fellow at the Department of Medical Physics, Virginia Commonwealth University, Richmond, VA, USA. He was the SBME Department Chairman, from 2013 to 2019. He is currently a Full Professor at the SBME Department, Cairo University. He has got 30 years of experience in academia and industry in the areas of multidimensional image analysis, pattern recognition, computer vision, and AI in medicine. He participated and lead the team who put a strategy and roadmap for digitally transforming health sector in Egypt (eHealth and comprehensive health insurance) via a grant from the National Telecommunication Regulation Authority (NTRA). He reviewed several papers with IEEE, IEEE/EMBC, and others. He is a Leader of Cairo University African Biomedical Engineering Mobility (ABEM) Program funded from European Union to seven African Universities. He received several awards, Egyptian State Award for research, in 2001, Cairo University Research Award, in 2002, and the IEEE/Senior Membership, in 2006. He chaired tens of session at IEEE conferences starting IEEE 2003 Midwest conference in circuits and systems. He was the Program Chair and the General Chair of the Cairo International Biomedical Engineering Conference (CIBEC08 and CIBEC14).

**ABDEL-MONEM M EL-SHARKAWY** (Member, IEEE) received the B.Sc. and M.Sc. degrees in systems and biomedical engineering (SBME) from Cairo University, Cairo, Egypt, and the M.Sc. and Ph.D. degrees in electrical and computer engineering from Johns Hopkins University (JHU), Baltimore, MD, USA, in 2004 and 2008, respectively. He worked as a Research Faculty Instructor at the Department of Radiology, JHU, from 2008 to 2014. He is currently an Associate Professor at SBME, Cairo University, and the Chairman of the National Academy of Information Technology for Person with Disabilities (NAID), Egyptian Ministry of Communications and Information Technology (MCIT). From 1998 to 2001, his research work was focused on ultrasound medical imaging related topics. He has been involved with magnetic resonance imaging (MRI) research, since 2002. His article on high field signal-to noise-ratio performance of the MR loopless antennas was featured as the cover picture for the May 2008 issue of the *Medical Physics* journal. He has about 23 peer-reviewed journal articles, three U.S. published patents, and more than 60 conference presentations. His current H-index is 15. His research interests include medical imaging, medical physics, computations and instrumentation, eHealth, digital transformation, and assistive technologies.